Tunable Transmissive Metastructure for Precise or Broadband Polarization Conversion Modulation Based on Graphene

Yu-Peng Li, Ke Xia, Lei Zhang, and Hai-Feng Zhang*

Based on the principle of Fabry–Perot (F–P) cavity resonance and the selective permeability of gratings to specific electromagnetic waves, a graphene-based metastructure (MS) is proposed for transmissive polarization conversion (PC). Using the full-wave numerical simulation, it is found that by varying the Fermi energy of graphene, the effective resonance range of the suggested MS can be dynamically adjusted from 0.47 to 0.348–0.714 THz, achieving the target of precise to ultra-broadband polarization modulation. In this paper, the plausibility of the structure is verified from multiple perspectives, and the correlation analyses of the electric and magnetic fields are the supporting illustrations. Additionally, the triggering mechanism of PC is visually illustrated in the study of the surface currents distributions. Simulation results reveal that the MS is superior in performance, functionality, and principle, and it is foreseen to hold excellent promise for integrated equipment in the terahertz (THz) band.

1. Introduction

The conventional methods for manipulating the polarization state of electromagnetic waves (EMWs) are to utilize the optical activity of chiral materials or the birefringence effect of anisotropic materials,[1,2] but the optical activity and birefringence presented in natural materials are pretty weak. In device design using natural materials, relatively thick dielectric substrates are generally required to meet the phase conditions for polarization conversion (PC), which discourages miniaturization and integration of the device. Nevertheless, metastructures (MSs), as 3D equivalents of metamaterials,[3,4] have provided a suitable solution to the above dilemma due to the unique physical properties such as negative refractive index and negative dielectric constant[5] and have attracted widespread interest.

The existing PC MSs are usually divided into the coss-PC (i.e., linear-to-linear PC) and linear-to-circular PC ones in function, as well as the reflective and transmissive ones in the propagation method. In the case of the reflective PC MSs, the incident wave tends to interfere with the reflected wave whose polarized direction has been converted, affecting the radiation performance of the device.[6] In contrast, transmissive PC MS does not suffer from the above-mentioned drawbacks. Thus, the transmissive PC MS research is even more pertinent to practical applications. Most transmissive PC MS continues two typical design approaches.[7–9] The first is the Fabry–Perot (F–P) cavity resonance of EMWs by combining orthogonal or deflected grating structures. In this way, the group led by Xiao[10] designed a multilayer structure consisting of two orthogonal sub-wavelength gratings and split ring resonators to achieve a 90° conversion of linear polarized waves in multiple bands. The second is through surface plasmon polariton (SPP) resonance for PC. For instance, Liu et al.[11] had applied the superposition of EMWs generated by SPP resonance to design a transmissive PC MS with a single metal slot layer operating in the terahertz (THz) band. In contrast, Chen et al.[12] combined the two concepts by inserting an arrowhead-shaped structure (enables multiple SPPs) into the orthogonal grating structures (implement F–P cavity resonance), which allows for a 3 dB bandwidth of 1:6.

As technology advances and the electromagnetic environment to which devices need to adapt gets progressively complex, the single-functional transmissive MSs gradually lose the significance of the research. Research into multifunctional tunable MSs enters a new boom. Based on the phase transition materials and the photosensitive materials, the group led by Prof. Zhang[13] published a photo-excited multitasking Janus MS in 2022, in which the VO_2 layer ensures the switching of transmission and reflection, while the adjustment of the operating band can be accomplished by regulating the power of the incident pump light. Li et al.[14] controlled the PIN tube via an independent external direct current (DC) bias network, and both reflection and transmission PCs can be realized. Zhu et al.[15] demonstrated that the phase-change material $Ge_2Sb_2Te_5$ can be incorporated in dielectric materials to achieve tunable and switchable linear polarization conversion in the telecom band. Moreover, numerous types exist in multifunctional MS, such as the gradual cross-polarization converter,[16] the hybrid metasurface with an

Y.-P. Li, K. Xia, L. Zhang, H.-F. Zhang
College of Electronic and Optical Engineering & College of Flexible Electronics (Future Technology)
Nanjing University of Posts and Telecommunications (NJUPT)
Nanjing 210023, P. R. China
E-mail: hanlor@njupt.edu.cn

**ADVANCED
SCIENCE NEWS**

www.advancedsciencenews.com

annalen
der **physik**

www.ann-phys.org

electrically biased silicon layer,[17] transmission-reflection-integrated coded MS,[18] frequency selective surface-polarization converter MS,[19] polarization converter-polarization separator MS,[20] etc.

In 2004, physicists K.S. Novoselov and A.K. Geim at Manchester University in the UK produced monolayer graphene by mechanical exfoliation.[21] Since then, much research in graphene has been conducted. Graphene is a 2D planar material consisting of monolayer carbon atoms arranged in a tight hexagonal lattice, and it is a semi-metallic thin film material with gapless energy bands.[22] Graphene features photovoltaic properties such as superior light transmission, ultra-wide response spectra, and fast photovoltaic response,[23] leading to significant research in frontier fields such as detection and photoelectric sensing.[24] Furthermore, graphene demonstrates exceptional capabilities in designing multifunctional tunable MS due to its conductivity which can be flexibly adjusted through the bias voltage.[25] Zhang et al.[26] in 2021, proposed a reflective MS with a hollow graphene resonant surface capable of broadband cross-PC and dual-frequency linear-to-circular PC functions at different Fermi energies. Zhao et al.[27] used the finite difference in time domain method to control linear asymmetric transmission and perfect PC on THz hybrid metallic graphene MS. The switching control is implemented by varying the graphene's Fermi energy (E_f) from 0.8 to 0 eV. Besides, Koijam Monika Devi et al.[28] showed that the Plasmon-induced transparency effect could be tuned by varying the Fermi energy of the graphene layer. Examples such as these are numerous, and various graphene-based metastructures have been investigated experimentally and theoretically including high-performance absorbers, cloaking, polarization control, wave front engineering, sensing, nonlinear optics, and lasing.[29] However, it is rare in the currently available research where graphene is combined with transmissive MS to realize PC modulation over different operating ranges.

This paper presents a multifunctional tunable transmissive MS based on graphene, which can perform different degrees of cross-PC in different ranges by tuning the E_f of the graphene. At $E_f = 0.1$ eV, precise and efficient modulation of EMWs can be obtained at 0.47 THz, with a polarization conversion rate (PCR) of 98.75%. While at $E_f = 1.0$ eV, PCR over 90% occurs in the range of 0.348–0.714 THz, at which point ultra-broadband modulation is achieved. The resonance structures of the MS consist primarily of mutually orthogonal gratings and two similar arrow-shaped resonant patches. The structure incorporates conventional operating mechanisms of both F–P cavity and SPP resonances, ensuring high efficiency and ultra-broadband. The selective permeability of graphene gratings for specific polarized waves is the key to implementing the dynamic range for PC. In summary, the described MS possesses multiple operating ranges compared to the single-band polarization converters. Both precise and ultra-broadband polarization modulation can be implemented in one single device. However, the MS benefits from dynamic tunability compared to conventional multi-operating band polarization converters, making the design more adaptable to the communication environment. Furthermore, graphene-specific electrical control methods are more accurate and accessible than most existing tuning techniques. And the transmissive mode of operation holds even greater fascination in practical applications. The suggested MS thus offers more unique advantages and a wider range of application scenarios in comparison to most available polarization converters. The device is potentially valuable for applications in electromagnetic steering, functional switching, wavefront detection, and holographic encryption[30,31] due to its excellent modulation efficiency and controllable modulation range.

2. Structure Design and Numerical Analysis

Figure 1 presents the specific structural design scheme for the given MS. By modulating the E_f of the graphene grating, the proposed MS can convert the incident y-polarized wave to the x-polarized wave and transmit it out of the array structure, as illustrated in Figure 1a. The DC bias voltage controlling the E_f is loaded on both the metal and the graphene gratings.[28,32] The external voltage application is more facilitated if the graphene grating is covered with an Indium Tin Oxide film.[28] Figure 1c is the stereoscopic view of the MS unit. To enhance the structural composition's visibility and intuitivity, the structure unfolds in the z-axis direction. As can be plainly seen from Figure 1c, three dielectric substrates with unequal thicknesses are separated by two arrow-shaped resonant patches whose structures are similar. Furthermore, gratings with the specific selectivity for polarized waves are placed at the top and bottom of the design. The modeling and performance analysis of the suggested MS is completed in the 3D electromagnetic simulation software HFSS, where the boundary condition is set to Master–Slave, and the Floquet port is positioned at the top of the unit to obtain the incident wave perpendicular to the MS.

More detailed information on MS units can be found in Figure 1d and **Table 1**. Three materials are used for the MS; the dielectric substrates are selected as Polyimide (lossy), whose relative permittivity is 3.5 and the loss tangent is 0.008.[33] Grating 1, as well as arrows 1 and 2, are made of gold (displayed as pink in the figures) with a conductivity of 4.561×10^7 S m^{-1}[34] and a thickness d_1 of 0.2 µm. The bottom grating structure (grating 2) consists of the graphite's single atomic layer, i.e., graphene ($d_2 = 0.34$ nm[35,36]); of note is that graphene is a 2D thin film structure formed by a monolayer of carbon atoms bonded in a honeycomb lattice, the structural characteristics of which are graphically illustrated in Figure 1b. Grating 1, located at the top of the unit, features five metal patches of length p and width m arranged at equal intervals along the y-axis; and grating 2, orthogonal to grating 1 in the structural arrangement, is positioned at the bottom of the MS. The arrow-shaped resonant patches can be constructed by cutting squares with a side length of 120 µm and combining them with rectangular strips of narrow dimensions. It is worth pointing out that a certain optical path difference exists when EMWs propagate and pass through different resonant layers in MS, while subtle differences in structural parameters for the arrow-shaped resonant patches can help to eliminate the adverse effects of the optical path difference.[37] Besides, the design concept of the arrow-shaped resonant structure symmetrical along the diagonal is more conducive to PC.[38]

The transmission and reflection process of EMWs between the gratings and the resonant layers are similar to a F-P cavity resonance. For the proposed MS, the selective permeability of the graphene grating directly affects the resonance effect. **Figure 2**a,b simulates the given MS for F–P cavity resonance at different Fermi energies, where **A** denotes the metal grating (grating
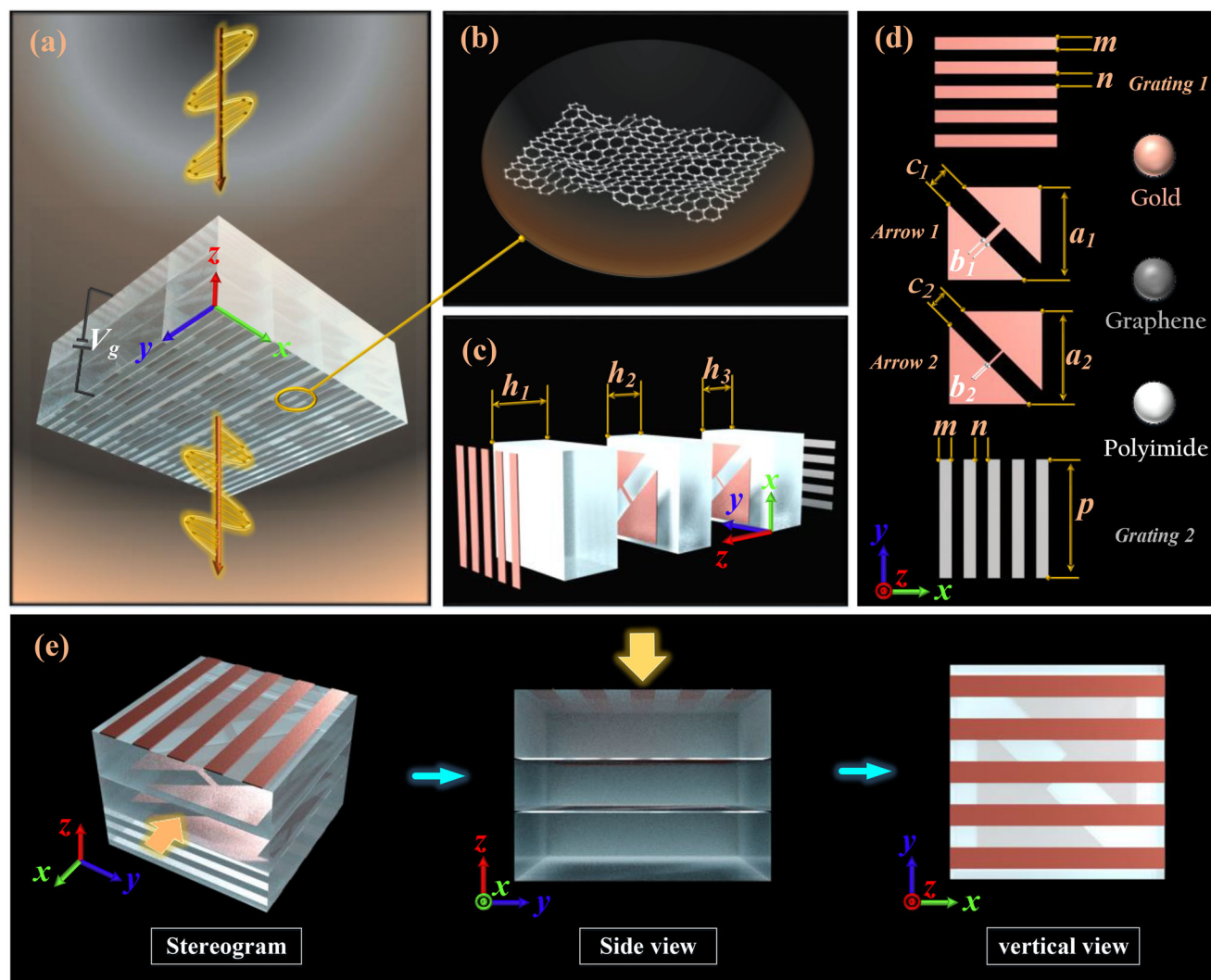
Figure 1. Schematic design of the given MS: a) 4×4 array structure diagram, b) graphene patches enlarged detail view, c) visualization of the unfolding unit, d) front view of resonant patches with structural parameters labeled, and e) 3D views.

Table 1. The detailed geometrical dimensions of the given MS.

Parameters	Values [µm]	Parameters	Values [µm]
a_1	120	d_1	0.2
a_2	120	d_2	0.00034
b_1	7	h_1	80
b_2	3	h_2	65
c_1	30	h_3	80
c_2	25	P	150
m	15	n	14

1), and **C** indicates the graphene grating (grating 2). At the same time, the double-layer arrow-shaped resonators between the two are summarized by **B-B** in a simplified way. When **C** is non-selective permeability, the F–P cavity resonance is predominantly concentrated between **A** and **B-B**, as illustrated in Figure 2a.

When the y-polarized wave incident into the cavity, reflected and transmitted waves of co-polarization and cross-polarization, respectively, are generated by **B-B**, where the transmitted wave will pass directly through **C** and no longer participate in resonance. In contrast, the reflected waves of x- and y-polarization will be retransmitted to **A**. Since **A** is selectively permeable to y-polarized waves, the y-polarized waves are transmitted out of **A**. The remaining x-polarized waves continue to participate in the intra-cavity resonance, repeating periodically.

When **C** is at $E_f = 1.0$ eV, the role of selective permeability for the F–P cavity resonance is demonstrated. Figure 2b highlights the resonance processes involved in the transmitted waves, which are formed by the EMWs passing through **B-B**. It should be declared that the reflected waves between **A** and **B-B** are still present but omitted in the plotting and description of Figure 2b since the resonance process remains the same as that described in Figure 2a. As Figure 2b demonstrates, when T_{xy} and T_{yy} through **B-B** arrive at **C**, **C** with selective permeability to x-polarized waves will screen the arriving EMWs. At this point, T_{xy} is transmitted

**ADVANCED
SCIENCE NEWS**

www.advancedsciencenews.com

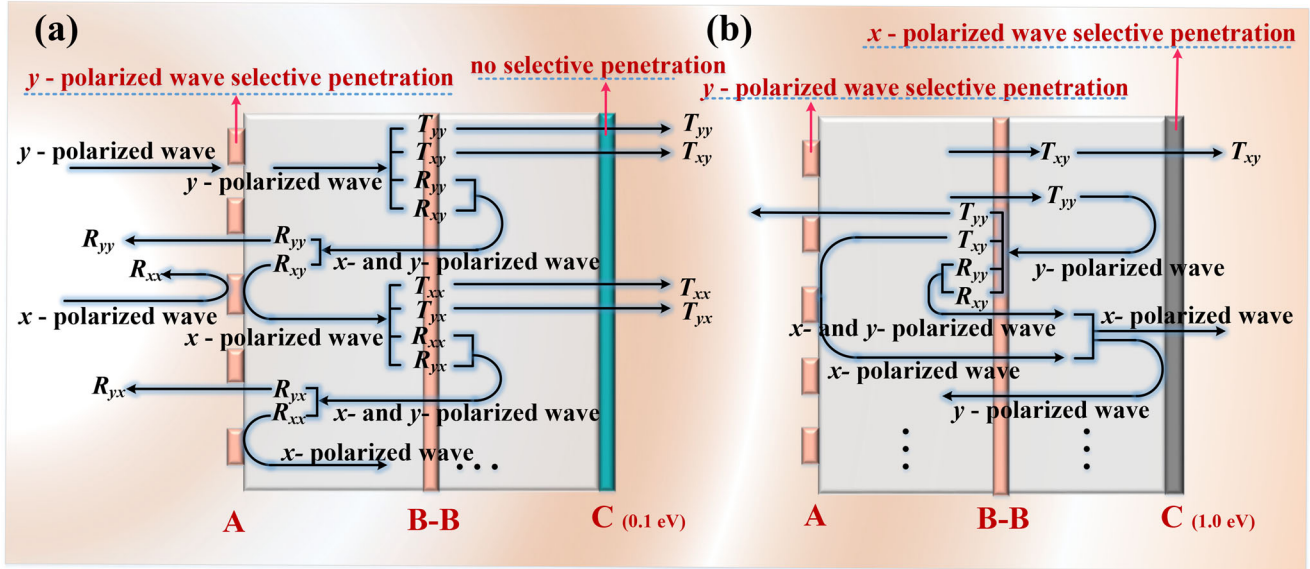annalen
der **physik**

www.ann-phys.org

Figure 2. Schematic diagram of the F–B cavity resonance at different states of structure **C**: a) $E_f = 0.1$ eV, b) $E_f = 1.0$ eV.

out of the MS, and T_{yy} is reflected into the cavity by **C** to participate in the F–P cavity resonance again. When the EMWs are re-transmitted from **C** to **B-B**, the resulting reflected waves R_{xy} and R_{yy} will remain in the interiors of **B-B** and **C** for resonance (the process similar to that described in Figure 2a). In contrast, the transmitted waves re-enter the interiors of **A** and **B-B**. The whole process is repeated. One can notice that when $E_f = 1.0$ eV, two F–P cavities are operating (**A** to **B-B** and **B-B** to **C**, respectively), and the double-layer cavity resonances are favorable to produce broadband effects because of the substantially increased utilization of the EMWs.

When the y-polarized wave is incident vertically along the $+z$-axis into the suggested MS, the incident electric field can be expressed as:

$$\vec{E}_i = E_i e^{j\phi_i}\hat{e}_y \tag{1}$$

where E_i and φ_i are the electric field amplitude and phase of the incident EMW, respectively, and $\hat{e}_y$ is the unit vector in the y-polarized direction. Correspondingly, the transmitted electric field can be expressed as:

$$\vec{E}_t = E_i T_{yy}\hat{e}_y + E_i T_{xy}\hat{e}_x = E_i t_{yy} e^{j\phi_{yy}}\hat{e}_y + E_i t_{xy} e^{j\phi_{xy}}\hat{e}_x \tag{2}$$

where T_{yy} and T_{xy} represent the transmission coefficients of the different polarized waves, while the corresponding transmission coefficient amplitudes and phases are denoted by (t_{yy} and t_{xy}) and (φ_{yy} and φ_{xy}), accordingly. Since MS is anisotropic, the amplitude and phase responses are in the orthogonal directions.

$$t_{yy} \rightarrow 0, t_{xy} \rightarrow 1 \tag{3}$$

$$\Delta\phi = \phi_{xy} - \phi_{yy} \rightarrow \pm(2n\pi + \pi) \tag{4}$$

The transmitted electric field can be simplified to Equation (5) when the amplitude and phase satisfy Equations (3) and (4), re-

spectively. From the perspective of formulae, it can be found that the y-polarized incident wave is converted into an x-polarized wave and transmitted out of the structure at this point.

$$\vec{E}_t = E_t e^{j\phi_t}\hat{e}_x \tag{5}$$

The PCR is typically used in the overall evaluation of MS, and the portion above 90% is the desired operating band. The propagation of EMWs is inevitably accompanied by certain losses, such as the absorption effect of the device on the waves. For polarization converters, high absorptivity (A) needs to be avoided. Therefore, for the MS analysis, the A is considered the significant loss of the device to the EMW.

$$PCR = \frac{t_{xy}^2}{r_{yy}^2 + r_{xy}^2 + t_{yy}^2 + t_{xy}^2} \tag{6}$$

$$A = 1 - (t_{xy}^2 + t_{yy}^2 + r_{xy}^2 + r_{yy}^2) \tag{7}$$

The performance analysis is done for the given MS based on the derivation above. **Figure 3**a depicts the amplitude variation of the transmission and reflection coefficients for $E_f = 0.1$ eV. It can be observed that t_{xy} peaks at 0.47 THz (with a value of 93.36%) and accompanies a rapid decrease in t_{yy} to a value of even <0.01. Meanwhile, the reflected waves, whether co-polarized or cross-polarized, are infinitely close to zero around the resonant frequency, which is considerable for transmissive PC, indicating that most EMWs are successfully transmitted to the other port. Figure 3c provides information on the phase difference, i.e., the phase difference of 184° is pretty close to the perfect phase condition at the cross-PC. It must be emphasized that the equations' derivation is based on the ideal and lossless conditions; the materials used in the actual design are lossy. The conditions of phase and amplitude are limited to an infinite approximation of the theoretical requirements, accompanied by a particular loss and the
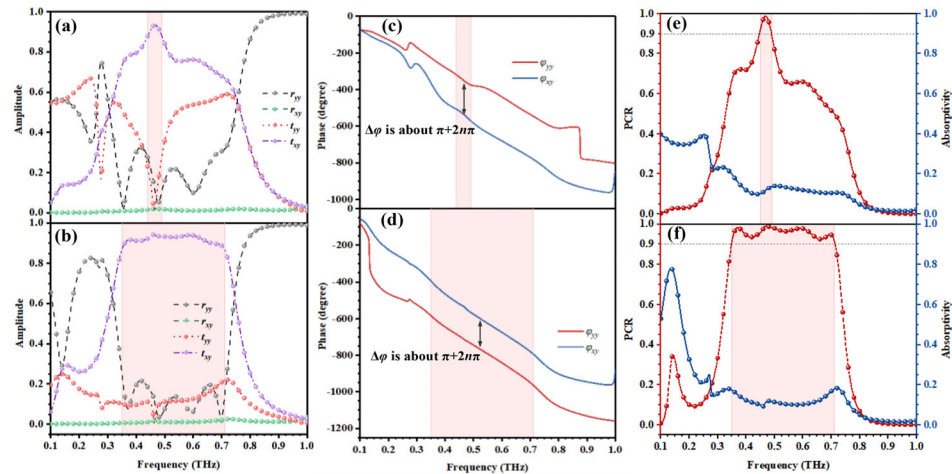
ADVANCED
SCIENCE NEWS

www.advancedsciencenews.com

annalen
der **physik**

www.ann-phys.org

Figure 3. When the E_f is at 0.1 and 1.0 eV, respectively: a,b) for the amplitude curves, c,d) for the phase curves, and e,f) for the performance curves.

fact that the PCR is not fully equal to 100%.[39,40] As seen in Figure 3e, the red curve represents the trend in PCR, and the blue curve depicts the A of the design. The PCR at 0.47 THz reaches 98.75% at $E_f = 0.1$ eV with the A of just 0.12, i.e., a superior and precise cross-PC is achieved at 0.47 THz.

Setting the E_f to 0.1 eV produces four resonant frequencies at 0.37, 0.47, 0.60, and 0.70 THz. As Figure 3b reveals, the x-polarized wave maintains over 90% transmittance in a particular band range, while the other coefficient amplitudes remain low, contributing to the formation of ultra-broadband. Meanwhile, within the above range, the phase difference is consistently fitted around ±180° and satisfies the phase condition. It is interesting to note that the deflected direction of φ_{xy} in Figure 3d is opposite to that of Figure 3c, and this discrepancy also emerges in the electric field distribution later on. The PCR calculated by Equation (6) is stable above 90% in the range of 0.348–0.714 THz with the relative bandwidth (RB) of 68.92% and, in particular, reached 98.13%, 98.90%, 97.94%, and 94.83%, respectively, at the four resonant frequencies. The lowest in-band loss (value of 0.09) occurs at 0.46 THz, also extremely close to the second resonant frequency as in Figure 3f, which means that the design features excellent PC efficiency combined with the efficient utilization for EMWs.

The selective penetrability of the grating for EMWs is particularly significant for the proposed MS. From the analysis of Figure 3 above, it can be seen that at $E_f = 0.1$ eV, a precise and high-efficiency PC is realized at 0.47 THz by the action of grating 1 and the two arrow-shaped resonant patches. However, **Figure 4**a simulates the structure without the gratings. The PCR curve (red) and the A curve (blue) reveal that the resonant frequency with the maximum PC efficiency is at 0.40 THz, where the PCR = 0.48 and the A remains low. However, obviously, this structure's shallow PCR peak is not compatible with the design goals of the polarization converter. The reason is that the reflected waves generated by the arrow-shaped patches at resonance no longer possess the ability to re-reflect and enter the resonant structure repeatedly. The process by which EMWs are continuously reflected and repeatedly incident into the resonant structure greatly reuses the EMWs, which is a critical factor in improving the PCR. In conclusion, the F–B cavity resonance effect has disappeared.

For the presented MS, the design of the double-layer arrow-shaped resonant patches is also essential. To prove this view, the deformed structure of the given MS is simulated. As illustrated in the structural schematic diagram on the right-hand side of Figure 4, arrow 1 is retained as the main resonant structure. Meanwhile, the distance between gratings is known to affect the operating effectiveness of the F–B cavity. To ensure a single study variable, the total thickness of the original dielectric substrates will be kept constant, so the thickness of both h_1 and h_3 will be adjusted to 112.5 μm. At this point, the performances of the structure at $E_f = 0.1$ eV and $E_f = 1.0$ eV are indicated in Figure 4b,c, respectively. Figure 4b shows that the structure reaches its highest PCR value at 0.36 THz, ≈67%, while Figure 4c demonstrates that the combined effect emerged by both the gratings and the resonant patch produces two main resonant frequencies at 0.37 and 0.51 THz, respectively. The expected broadband trend in the range of 0.35–0.52 THz is primarily achieved. Nevertheless, the comparison with the PCR curves in Figure 3f reveals that the design of the double-layer arrow-shaped resonant patches contributes to the broadening of the operating band. Generally, more resonant layers result in an inevitable increase in the number of resonant frequencies (from two to four in the above condition), which is one of the main ways to increase the bandwidth. Therefore, the structural design of the double-layered arrow-shaped resonant patches can prove advantageous. In addition, the discussion of the magnetic field distribution and the surface currents distribution of the suggested MS can also corroborate the conclusion laterally.

The principles of PC from the views of magnetic field and surface currents distributions are explained as follows. The surface currents distribution at 0.37 THz ($E_f = 1.0$ eV) is presented as an example. **Figure 5**a displays the magnetic field distribution in the zoy plane. The vital part of the magnetic field energy converges mainly between the two layers of the arrow-shaped resonant patches, which can be explained by the surface currents distribution. Define the upper surface of arrow 1 as "Z_1+" and its lower surface as "Z_1-", and similarly, the upper and lower surfaces of arrow 2 to be "Z_2+" and "Z_2-", as seen in Figure 5a, separately. The surface currents distributions of arrows 1 and 2 in the yox plane are presented in Figure 5b–e as the 2 × 2 arrangements. The

ADVANCED
SCIENCE NEWS
www.advancedsciencenews.com
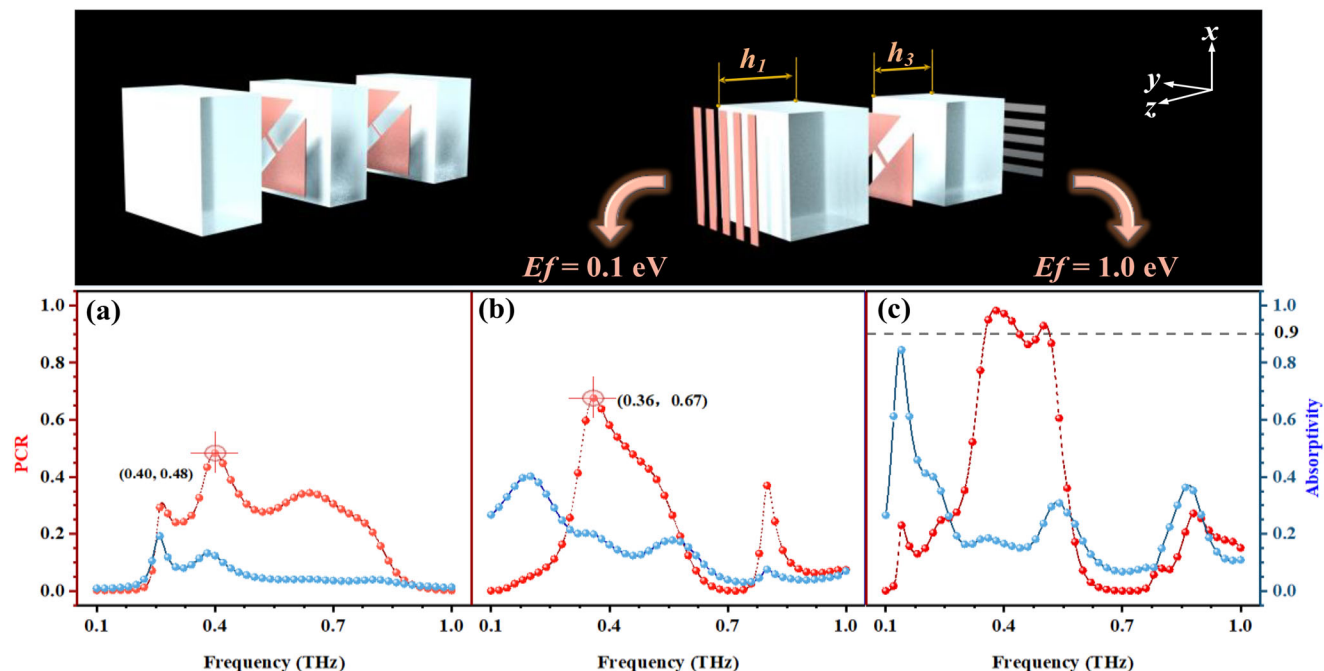
annalen
der **physik**
www.ann-phys.org

Figure 4. a) Performance curves without grating 2, b,c) performance curves at different Fermi energies when the structure features a single-layer arrow-shaped resonant patch, respectively.
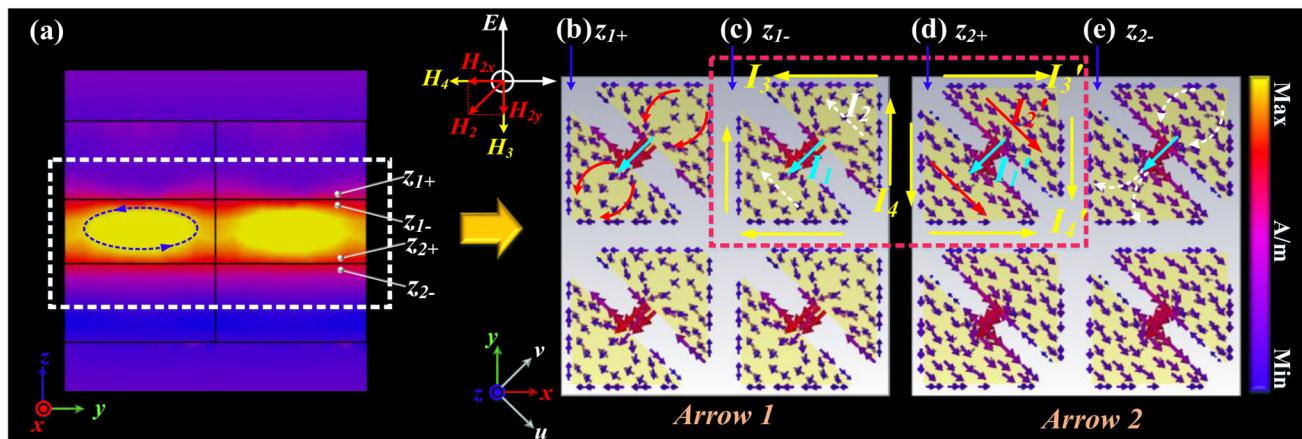

Figure 5. When $E_f = 1.0$ eV at 0.37 THz, a) the magnetic field distribution, and b–e) the surface current distributions on different faces of the resonant patches.

red solid arrows mark the current directions on "Z_i+" while the current distributions on "Z_i-" are highlighted with white dashed arrows. Focusing on the current distributions on the "Z_1-" and "Z_2+" marked by the red dashed box, a large amount of current I_1 toward the -v-axis converges at the connection in the center of arrow 1 and is accompanied by a great deal of energy as seen in Figure 5c. Moreover, in Figure 5d, the isotropic currents I_1' corresponding to I_1 are present, and electrical resonance is generated when the surface currents in the same direction respond to each other. The more surface currents on the arrow-shaped resonant patches operate in a magnetically resonant manner. By carefully observing that the current I_2 flowing along the -u-axis on "Z_1-" is in the exact opposite direction to the current I_2' on "Z_2+", thus,

the circulating currents are generated; according to the right-hand rule, the circulating current produces the corresponding magnetic dipole m_2 with the related magnetic field H_2 oriented toward the -v-axis. By decomposition, the H_2 can be converted into components H_{2x} and H_{2y}, while the magnetic field component parallel to the electric field takes the core force for the PC. Similarly, the currents at the edges of the arrow-shaped resonant patches (I_3 corresponding to I_3' and I_4 corresponding to I_4') can be analyzed. To summarize, multiple circulating currents are present between the "Z_1-" and "Z_2+" of the arrow-shaped resonant patches, resulting in a superposition of magnetic energy, with the eligible magnetic field components triggering the PC.
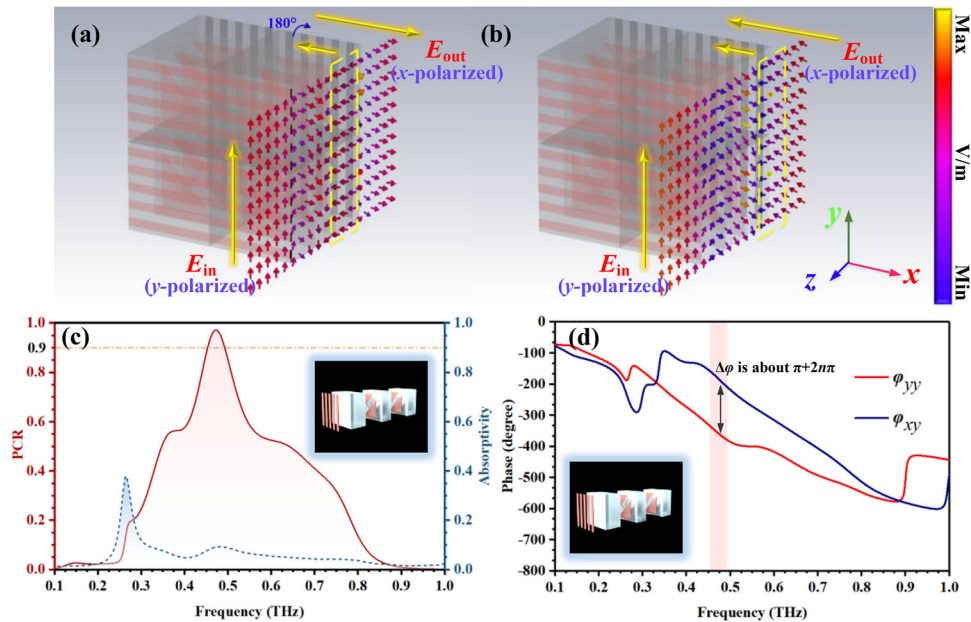
Figure 6. Schematic diagram of the variation in electric field direction for a) $E_f = 0.1$ eV at 0.47 THz, b) $E_f = 1.0$ eV at 0.37 THz; c) performance curves and d) phase for structure without grating 2 when $E_f = 0.1$ eV at 0.47 THz.

To better understand and visualize the process of PC, the electric field distribution of the EMW as it passes through the MS is shown in **Figure 6**. In particular, Figure 6a depicts the *yoz* cross-section of the field distribution with $E_f = 0.1$ eV at 0.47 THz. The electric field direction of the incident wave is along the +*y*-axis; as it travels through the two layers of arrow-shaped resonant patches sequentially, the electric field direction is deflected in varying degrees, indicating that the polarized direction is changed. The cross-PC phenomenon is fully established when the EMW completely passes through arrow 2, at which point the electric field polarization direction is along the -*x*-axis. However, when the EMW goes through grating 2, the electric field direction is deflected by 180° so that the electric field direction is along the +*x*-axis. The above indicates that when the presented MS operates at 0.47 THz, the two layers of arrow-shaped resonant patches play the primary resonant role, the same as that obtained from the analysis presented in the previous section. The grating 2 offers no selective penetrability when the E_f of graphene is at 0.1 eV. Instead, the designed grating 2 acts as a correction for the phase deflection direction to some extent, directly leading to a change in the electric field direction. Figure 6c,d presents the performance and phase curves of the proposed MS without grating 2, directly confirming the above conclusions. It can be found that the structure maintains excellent and precise modulation at 0.47 THz (PCR = 97.15%) while achieving a phase difference of 176° to meet the phase requirements of the PC. It demonstrates that when the EMW passes through grating 1, arrow 1, and arrow 2, the PC remains essentially the same as the original design. Nevertheless, comparing Figures 3c and 6d, it is evident that the structure without grating 2 has a significant phase deviation at low frequencies for φ_{xy}, which is corrected in the given MS. This process is perfectly reflected in the variation of the electric field direction in Figure 6a. Phase is a critical performance indicator for polarization converters, and guarantee-

ing phase stability is essential. As Figure 6a reveals, eventually, when the suggested MS performs a precise PC for the EMW, the *y*-polarized wave can be perfectly converted into an *x*-polarized wave, i.e., when $E_f = 0.1$ eV, the design achieves a PCR of 98.75% at 0.47 THz.

The 0.37 THz is selected as the representative resonant frequency for $E_f = 1.0$ eV, as illustrated in Figure 6b. When the *y*-polarized EMW is incident inside the proposed MS, due to the interlayer coupling generated at resonant frequencies, the field modes are warped to different degrees as the wave passes through the different resonant layers. Before the EMWs arrive at grating 2, the electric field direction has almost completed the conversion toward the -*x*-axis, but a few EMWs are still polarized in some haphazard directions. As the graphene grating features selective permeability to *x*-polarized waves, in this case, the polarized waves that satisfy the conditions are transmitted, fulfilling the design goal of cross-PC. It is worth noting that the electric field direction of the outgoing EMW at 0.37 THz (representing the case of $E_f = 1.0$ eV) is exactly opposite to that at 0.47 THz (representing the case of $E_f = 0.1$ eV). However, both are *x*-polarized waves (representing the success of the PC), while the different steering of φ_{xy} in Figure 3c,a reasonably echoes and explains the phenomenon. The analysis of the remaining resonant frequencies that produce the broadband effect is identical to the above, therefore not repeated. The ultra-broadband cross-PC function is ultimately achieved in the range of 0.348–0.714 THz when $E_f = 1.0$ eV.

As the EMW propagates through the two-layer grating structures, the selective permeability can be reflected by the distribution of the electric field energy, as proven in **Figure 7**. The distribution of the electric field energy at $E_f = 0.1$ eV (for 0.47 THz) and $E_f = 0.1$ eV (for 0.37 THz) are discussed, respectively. As gratings 1 and 2 are orthogonally aligned in orientation, observations from each direction will be made, where the white-dashed boxes
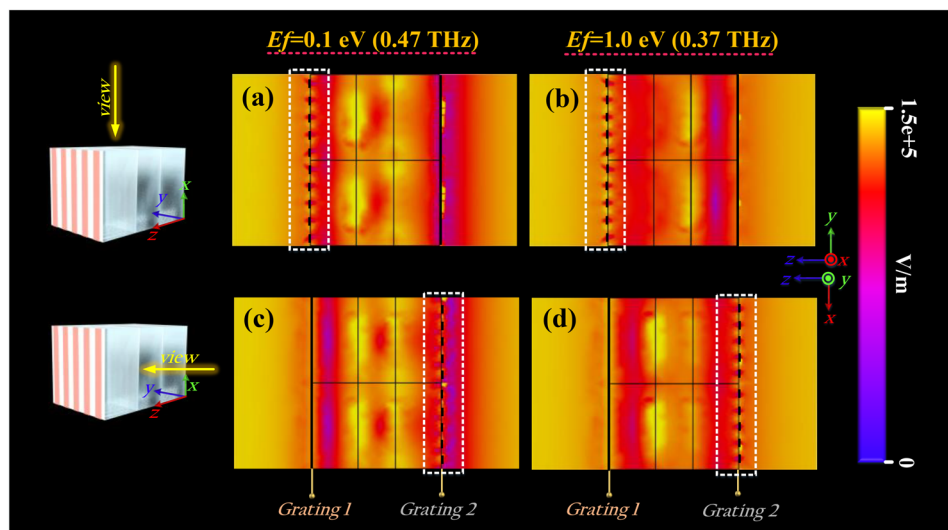
ADVANCED
SCIENCE NEWS

www.advancedsciencenews.com

annalen
der **physik**

www.ann-phys.org

Figure 7. Electric field energy distribution diagrams of the described MS at different Fermi energies from different viewing directions: a) $E_f = 0.1$ eV (0.47 THz) and b) $E_f = 1.0$ eV (0.37 THz) when looking toward the structure along the x-axis; c) $E_f = 0.1$ eV (0.47 THz), and d) $E_f = 1.0$ eV (0.37 THz) when looking toward the structure along the y-axis.
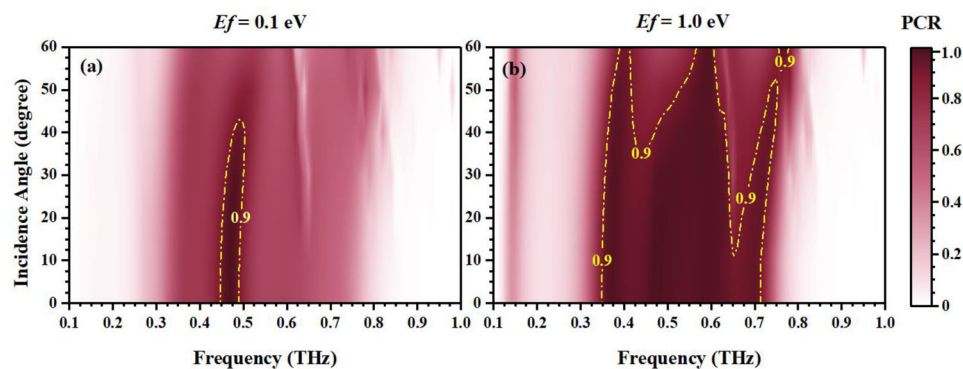

Figure 8. Angular stability when the E_f is set to a) 0.1 and b) 1.0 eV, respectively.

highlight the energy distributions around the gratings. Looking along the x-axis toward the MS units, it can be noticed that grating 1 is equally spaced. Since the metal grating blocks the EMWs propagation to a certain extent, it can be found in Figure 7a,b that the electric field energy is weaker where the metal grating strip patches are located, showing the purple or red color. On the contrary, the energy between the grating strip patches is intense since the EMW satisfying the incident conditions enters the resonant unit from here. At this point, the electric field energy exhibits an interlaced intensity dependent on the layout of the grating 1, regardless of whether the E_f is set to 0.1 or 1.0 eV. When the MS units are observed from the y-axis direction, it can be observed that the energy around the graphene grating presents various states due to the different Fermi energies. At $E_f = 0.1$ eV, grating 2 at 0.47 THz no longer features interlaced energy distribution but transmits EMWs relatively uniformly, as shown in Figure 7c, owing to the failure of the selective permeability of grating 2 to EMWs at low E_f. However, as the E_f of graphene rises to 1.0 eV, grating 2 displays the desired selective permeability; as seen in Figure 7d, when the design is operated at 0.37 THz, the energy

intensity is interlaced according to the distribution of grating 2, which is the same as grating 1.

In increasingly complex communication environments, ensuring that the incident EMW is perpendicular to the MS at all times is challenging. Besides, excellent angular stability makes the device more suitable for comprehensive applications such as wavefront detection, so the ability to adapt to extensive angular incidence is particularly critical. **Figure 8** demonstrates the angular stability when the suggested MS is in the precise or broadband modulation. When the E_f is adjusted to 0.1 eV, the design achieves the PC efficiency of over 90% in the narrow band of 0.44–0.49 THz, with a peak PCR at 0.47 THz (98.75%). The above properties remain essentially stable at incidence angles <40°, accompanied merely by a slight blueshift, as demonstrated in Figure 8a. When the E_f is set to 1.0 eV, the broadband effect remains stable up to 10°. It deteriorates at 0.65 THz when the incidence angle exceeds 10°, and the resonant frequency, initially at 0.70 THz, starts to blueshift continuously. As the incidence angle increases, the 0.47 THz resonant frequency moves toward 0.60 THz. The 0.37 THz resonant frequency, which is only
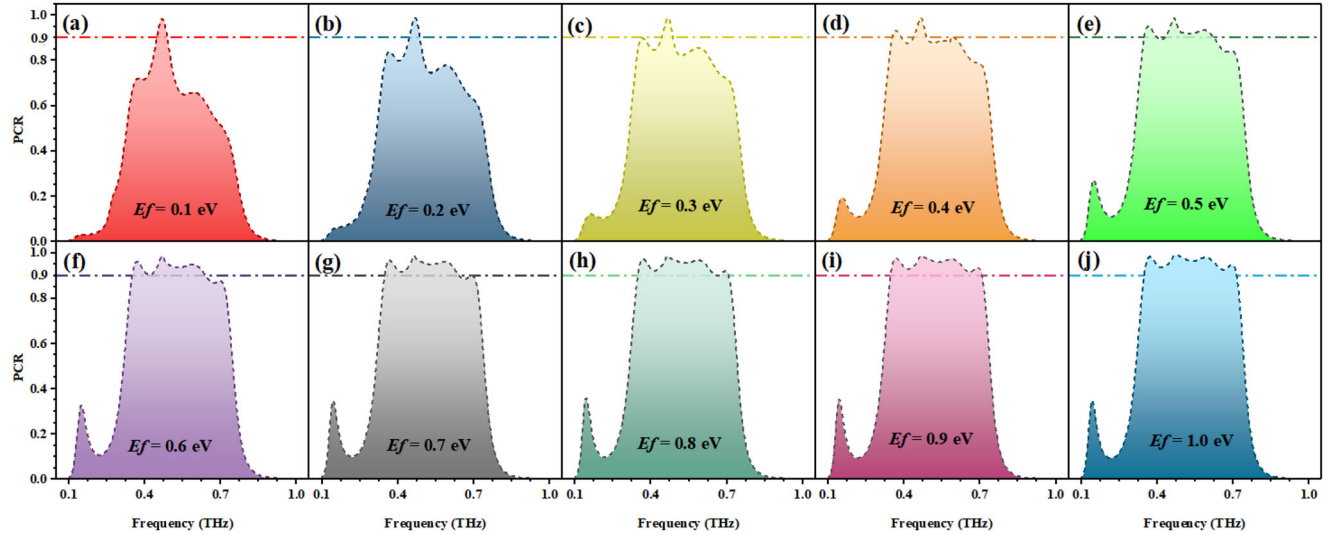
**ADVANCED
SCIENCE NEWS**

www.advancedsciencenews.com

**annalen
der physik**

www.ann-phys.org

Figure 9. a–j) Variation in PCR as the E_f changes from 0.1 to 1.0 eV.

slightly blueshifted, is separated from the 0.47 THz resonant frequency by a growing distance, causing the PCR to become depressed between the two. The original excellent broadband effect gradually disappears when the incidence angle is >30°.

The planar conductivity of graphene is related to the E_f transferred by electron or chemical doping. The complex conductivity σ_s is the sum of the intra-band leap σ_{intra} and inter-band leap σ_{inter} in graphene. According to the Kubo formula,[41,42] the specific conductivity is calculated as Equations (8)–(10):

$$\sigma_{intra}\left(\omega, E_f, \Gamma, T\right) = -j\frac{e^2 k_B T}{\pi \hbar^2(\omega\text{-}j2\Gamma)}\left(\frac{E_f}{k_B T} + 2\ln(e^{-E_f/k_B T} + 1)\right)$$

(8)

$$\sigma_{inter}\left(\omega, E_f, \Gamma, T\right) = \frac{-je^2}{4\pi\hbar}\ln\left(\frac{2\left|E_f\right| - (\omega\text{-}j2\Gamma)\hbar}{2\left|E_f\right| + (\omega\text{-}j2\Gamma)\hbar}\right)$$

(9)

$$\sigma_S = \sigma_{intra}\left(\omega, E_f, \Gamma, T\right) + \sigma_{inter}\left(\omega, E_f, \Gamma, T\right)$$

(10)

where E_f denotes the Fermi energy, $\bar{h}=h/2\pi$ represents Planck's constant, and k_B and e are the Boltzmann constant and the electron's charge, respectively. The ambient temperature T is typically set to 300 K with $\omega = 2\pi f$ as the angular frequency, the electron-phonon relaxation time $\tau = 0.1$ ps, and its associated phenomenological scattering rate $\Gamma = 1/2\tau$. The voltage can be applied to the graphene by adding a bias gate control structure, thus achieving effects on the control of the E_f and thus regulating the operating state of the given MS. Typically, the E_f of graphene varies in the range of 0.1–1.0 eV. When the DC bias voltage controls the conductivity of graphene, the relationship between the bias voltage V_g and the E_f can be expressed by the approximate closed formula:[43]

$$E_f \approx \hbar v_f \sqrt{\frac{\pi \varepsilon_r \varepsilon_0 V_g}{e t_s}}$$

(11)

For the proposed MS, the trend of the PCR as the E_f changes from 0.1 to 1.0 eV is illustrated in **Figure 9**. When the E_f is adjusted to 0.1 eV, the suggested MS exhibits an intensive PC at 0.47 THz with PCR = 98.75%. Meanwhile, the PCR curve implicitly shows a tendency for broadband PC effects to develop at low and high frequencies. At $E_f = 0.2$ eV, the resonant frequencies at 0.37 and 0.60 THz come to the fore, with PCR of 83.55% and 77.82%, separately. As the E_f rises to 0.5 eV, the broadband effect of the described MS gradually appears with the emergence of 0.70 THz resonant frequency (PCR = 84.05%). At the same time, the PCR at low and medium resonant frequencies also remains above 90% due to the increasing resonance, while the 0.70 THz resonant frequency also reaches the same effect at $E_f = 0.8$ eV. At $E_f = 1.0$ eV, the broadband effect is created by the combined action of the four resonant frequencies, and the given MS maintains a stable PCR above 90% in the range of 0.348–0.714 THz, in line with the expected design goal of efficient and wide-range PC at $E_f = 1.0$ eV. Observing the tendency of the curves in Figure 9, it can be seen that the variations in E_f lead to the changes in the operating characteristics of grating 2, resulting in the increasing F–P cavity resonance, which possesses a significant effect on the resonant frequencies at 0.37, 0.60, and 0.70 THz. However, the 0.47 THz resonant frequency is mainly induced by the double-layer arrow-shaped resonant patches (as seen in the previous section), and the change in the operating characteristics of grating 2 possesses weak effects on this frequency.

The structural parameters are usually closely related to the freedom of design and fabrication tolerance, so it is essential to discuss the structural parameters that significantly influence the device. For the presented MS, the edge length a_2 of arrow 2 is discussed. As displayed in **Figure 10**, a_2 varies from 108 to 132 μm with a span of 6 μm in the $E_f = 0.1$ eV and $E_f = 1.0$ eV cases, correspondingly. At $E_f = 0.1$ eV with $a_2 = 108$ μm, the PCR at 0.46 THz is approaching 100%. At the same time, this resonant frequency is slightly blueshifted with increasing a_2 and accompanied by a decrease in conversion efficiency. At $a_2 = 132$ μm, this resonant frequency reaches a PCR of 91.56% at 0.48 THz. During this process, the resonant point originally located at 0.62 THz in
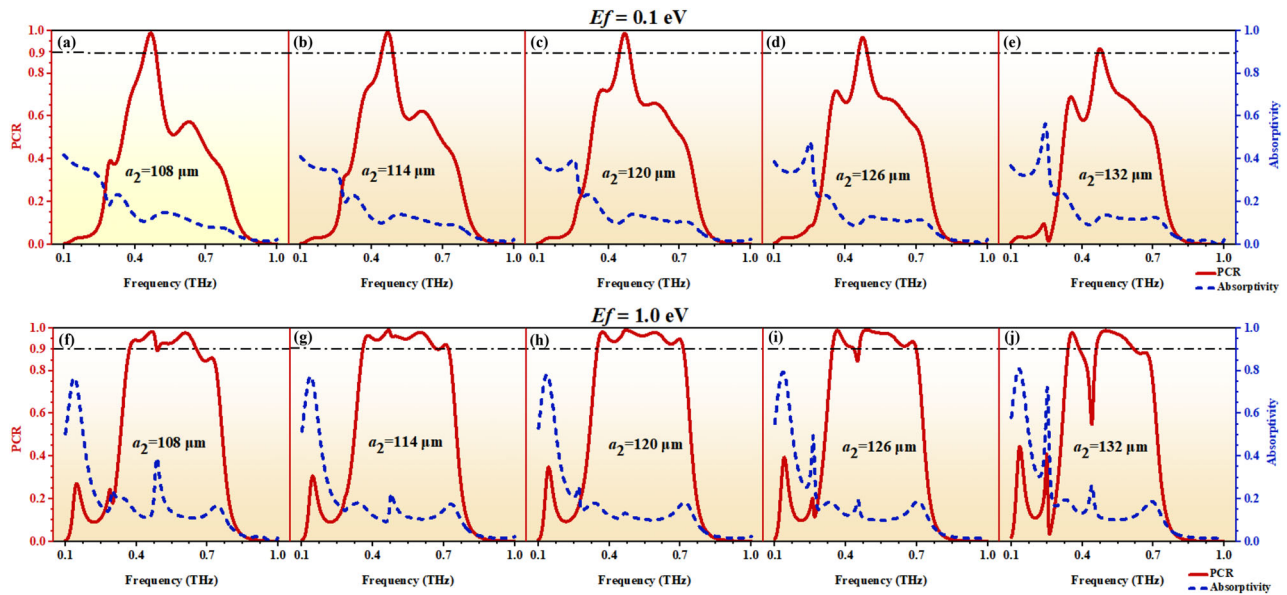
Figure 10. Performance curves with a_2 for a–e) $E_f = 0.1$ eV and f–j) for $E_f = 1.0$ eV.

Figure 10a is continuously redshifted. In contrast, a fresh resonant point is gradually split out at the lower frequency of the PCR peak, which is eventually situated at 0.35 THz in Figure 10e. Observing Figure 10a–e, around the resonant frequency where the PCR peak is located, the A of the proposed MS to the EMW remains constant and low.

In contrast, the variation in a_2 significantly impacts device losses at $E_f = 1.0$ eV. Except for the case of $a_2 = 120$ μm, the other values assigned all result to a_2 in a A peak above 20% near 0.47 THz, e.g., the A is 0.39 at 0.48 THz in Figure 10f, and it is 0.26 at 0.44 THz in Figure 10j. More obviously, the value of a_2 is dramatically influential on the second resonant frequency (located at 0.47 THz in the MS), especially when $a_2 = 132$ μm, where the resonant point is redshifted to 0.44 THz and accompanied by only 55.94% PCR, exhibiting a sharp and deep PCR depression in Figure 10j. Given the above analysis, $a_2 = 120$ μm is chosen as the optimal value. At low Fermi energy ($E_f = 0.1$ eV), the PCR peak at 0.47 THz is maintained at 98.75% and is accompanied by an EMW loss of only 0.12. Furthermore, at high Fermi energy ($E_f = 1.0$ eV), the PCR of over 90% with an A of <0.2 is sustained in the ultra-broadband of 0.348–0.714 THz.

3. Conclusion

In summary, we propose a MS which can realize different ranges of EMW polarization modulation by adjusting the E_f of graphene. The precise and efficient PC occurs at 0.47 THz when $E_f = 0.1$ eV, while at $E_f = 1.0$ eV, the polarization effect extends to 0.348–0.714 THz and is accompanied by RB of 68.92%. The detailed analyses presented in the paper are for the F–P cavity and the selective permeability of the gratings, which are visualized in the electric and magnetic fields. Furthermore, the conventional angular stability analysis and parametric discussions also inform the practical application of the MS. The transmissive PC MS is principled and practical, and will be of value in the design and application of transmissive THz devices.

Conflict of Interest

The authors declare no conflict of interest.

Data Availability Statement

The data that support the findings of this study are available on request from the corresponding author. The data are not publicly available due to privacy or ethical restrictions.

[1] M. Kuwata-Gonokami, N. Saito, Y. Ino, M. Kauranen, K. Jefimovs, Tuomas, *Phys. Rev. Lett.* **2005**, *95*, 227401.

[2] Y. Joly, S. P. Collins, S. Grenier, H. C. N. Tolentino, M. D. Santis, *Phys. Rev. B* **2012**, *86*, 220101.

[3] Y. P. Li, L. Zeng, H. F. Zhang, D. Zhang, K. Xia, L. Zhang, *Opt. Express* **2022**, *30*, 34586.

[4] P. F. Qiao, W. J. Yang, C. J. Chang-Hasnain, *Adv. Opt. Photon.* **2018**, *10*, 180.

[5] H. R. Chen, Y. Z. Cheng, J. C. Zhao, X. S. Mao, *Mod. Phys. Lett. B* **2018**, *32*, 1850366.

[6] X. Gao, X. Han, W. P. Cao, H. O. Li, H. F. Ma, T. J. Cui, *IEEE Trans. Antennas Propag.* **2015**, *63*, 3522.

[7] R. Orr, G. Goussetis, V. Fusco, *IEEE Trans. Antennas Propag.* **2013**, *62*, 19.

[8] P. Xie, G. M. Wang, H. P. Li, J. G. Liang, X. J. Gao, *IEEE Trans. Antennas Propag.* **2019**, *68*, 3213.

[9] Y. F. Li, Y. Q. Pang, J. F. Wang, Q. Q. Zheng, M. C. Feng, H. Ma, J. Q. Zhang, Z. Xu, S. B. Qu, *Phys. Rev. Appl.* **2018**, *10*, 064002.

[10] D. J. Liu, Z. Y. Xiao, X. L. Ma, Z. H. Wang, *Opt. Commun.* **2015**, *354*, 272.

[11] W. W. Liu, S. Q. Chen, Z. C. Li, H. Cheng, P. Yu, J. X. Li, J. G. Tian, *Opt. Lett.* **2015**, *40*, 3185.

[12] H. Y. Chen, H. Ma, J. F. Wang, S. B. Qu, Y. Q. Pang, M. B. Yan, Y. F. Li, *Appl. Phys. A* **2016**, *122*, 122.

[13] Z. H. Guo, Y. Z. Sun, L. Zeng, H. F. Zhang, *Ann. Phys.* **2022**, *534*, 2100499.

[14] Y. Li, Y. Wang, Q. S. Cao, *IEEE Access* **2019**, *7*, 129183.

[15] W. Zhu, R. S. Yang, Y. C. Fan, Q. H. Fu, H. J. Wu, P. Zhang, N. H. Shen, F. L. Zhang, *Nanoscale* **2018**, *10*, 12054.

[16] J. M. Rao, R. Sarkar, G. Kumar, *OSA Continuum* **2019**, *2*, 603.

[17] R. S. Yang, J. Lou, F. L. Zhang, W. Zhu, J. Xu, T. Cai, Q. H. Fu, H. Q. Li, Y. C. Fan, *Adv. Photon. Res.* **2021**, *2*, 2100103.

[18] L. Zhang, R. Y. Wu, G. D. Bai, H. T. Wu, Q. Ma, X. Q. Chen, T. J. Cui, *Adv. Funct. Mater.* **2018**, *28*, 1802205.

[19] L. L. Wang, S. B. Liu, X. K. Kong, H. F. Zhang, Q. M. Yu, Y. D. Wen, D. D. Wang, *IEEE Trans. Antennas Propag.* **2020**, *69*, 2833.

[20] Y. Li, Q. S. Cao, Y.i Wang, *IEEE Antennas Wirel. Propag. Lett.* **2018**, *17*, 1314.

[21] A. K. Geim, K. S. Novoselov, *Nat. Mater.* **2007**, *6*, 183.

[22] Y. F. Ren, Z. H. Qiao, Q. Niu, *Rep. Prog. Phys.* **2016**, *79*, 066501.

[23] J. Z. Fang, Z. Q. Zhou, M. Q. Xiao, Z. Lou, Z. M. Wei, G. Shen, *InfoMat* **2020**, *2*, 291.

[24] E. W. Hill, A. Vijayaragahvan, K. Novoselov, *IEEE Sens. J.* **2011**, *11*, 3161.

[25] F. Chen, Y. Z. Cheng, H. Luo, *Materials* **2020**, *13*, 860.

[26] H. J. Zhang, Y. Liu, Z. Q. Liu, X. S. Liu, G. Q. Liu, G. L. Fu, J. Q. Wang, Y. Shen, *Opt. Express* **2021**, *29*, 70.

[27] J. X. Zhao, J. L. Song, T. Y. Xu, T. X. Yang, J. H. Zhou, *Opt. Express* **2019**, *27*, 9773.

[28] K. M. Devi1, M. Islam, D. R. Chowdhury, A. K. Sarma, G. Kumar, *Europhys. Lett.* **2018**, *120*, 27005.

[29] C. Fan, N. H. Shen, F. L. Zhang, Q. Zhao, H. J. Wu, Q. H. Fu, Z. Y. Wei, H. Q. Li, C. M. Soukoulis, *Adv. Opt. Mater.* **2019**, *7*, 1800537.

[30] P. Yu, J. X. Li, S. Zhang, Z. W. Jin, G. Schütz, C. W. Qiu, M. Hirscher, N. Liu, *Nano Lett.* **2018**, *18*, 4584.

[31] L. Bao, T. J. Cui, *Microw. Opt. Technol. Lett.* **2020**, *62*, 9.

[32] N. Kakenov, O. Balci, T. Takan, V. A. Ozkan, H. Altan, C. Kocabas, *ACS Photon.* **2016**, *3*, 1531.

[33] S. Anand, D. S. Kumar, R. J. Wu, M. Chavali, *Optik* **2014**, *125*, 5546.

[34] J. Yang, C. Gong, L. Sun, P. Chen, L. Lin, W. W. Liu, *Sci. Rep.* **2016**, *6*, 39732.

[35] J. F. Shen, Y. Z. Hu, M. Shi, X. Lu, C. Qin, C. Li, M. X. Ye, *Chem. Mater.* **2009**, *21*, 3514.

[36] P. K. Maharana, P. Padhy, R. Jha, *IEEE Photon. Technol. Lett.* **2013**, *25*, 2156.

[37] N. M. D'souza, V. Mathew, *Opt. Laser Technol.* **2016**, *80*, 214.

[38] C. Huang, Y. J. Feng, J. M. Zhao, Z. B. Wang, T. Jiang, *Phys. Rev. B* **2012**, *85*, 195131.

[39] W. L. Guo, G. M. Wang, K. Chen, H. P. Li, Y. Q. Zhuang, H. X. Xu, Y. J. Feng, *Phys. Rev. Appl.* **2019**, *12*, 014009.

[40] L. X. Liu, X. Q. Zhang, M. Kenney, X. Q. Su, N. N. Xu, C. M. Ouyang, Y. L. Shi, J. G. Han, W. L. Zhang, S. Zhang, *Adv. Mater.* **2014**, *26*, 5031.

[41] G. W. Hanson, *J. Appl. Phys.* **2008**, *103*, 064302.

[42] Y. Zhang, Y. J. Feng, J. M. Zhao, *Carbon* **2020**, *163*, 244.

[43] J. S. Gómez-Díaz, J. Perruisseau-Carrier, *Opt. Express* **2013**, *21*, 15490.